Guo *et al.*
Protection and Control of Modern Power Systems (2022) 7:40
https://doi.org/10.1186/s41601-022-00261-y

Protection and Control of Modern Power Systems

ORIGINAL RESEARCH Open Access

Online estimation of SOH for lithium-ion battery based on SSA-Elman neural network

Yu Guo[1], Dongfang Yang[2], Yang Zhang[3], Licheng Wang[4] and Kai Wang[1*]

Abstract

The estimation of state of health (SOH) of a lithium-ion battery (LIB) is of great significance to system safety and economic development. This paper proposes a SOH estimation method based on the SSA-Elman model for the first time. To improve the correlation rates between features and battery capacity, a method combining median absolute deviation filtering and Savitzky–Golay filtering is proposed to process the data. Based on the aging characteristics of the LIB, five features with correlation rates above 0.99 after data processing are then proposed. Addressing the defects of the Elman model, the sparrow search algorithm (SSA) is used to optimize the network parameters. In addition, a data incremental update mechanism is added to improve the generalization of the SSA-Elman model. Finally, the performance of the proposed model is verified based on NASA dataset, and the outputs of the Elman, LSTM and SSA-Elman models are compared. The results show that the proposed method can accurately estimate the SOH, with the root mean square error (RMSE) being as low as 0.0024 and the mean absolute percentage error (MAPE) being as low as 0.25%. In addition, RMSE does not exceed 0.0224 and MAPE does not exceed 2.21% in high temperature and low temperature verifications.

Keywords: Lithium-ion battery, State of health, Data-driven, SSA-Elman

1 Introduction

Renewable energy has attracted much attention because of sustainable development issues [1–4]. LIBs are widely used in both military and civil fields because of their high energy density, high rated voltage, strong adaptability to high and low temperatures and low cost. Accurate estimation of SOH is of great significance to improving LIB safety and service life [5, 6], as well as improving the efficiency of the LIB and reduce equipment operating costs [7]. From the SOH of the LIB, the aging degree of the LIB can be detected to assess any safety risks and determine when the battery needs to be replaced. This can bring huge benefits [4].

So far, many related studies have proposed a variety of methods to estimate the SOH of an LIB from multiple angles. The methods can be divided into direct measurement, model-based and data-based methods. The direct measurement method is to use precise instruments to measure the open circuit voltage (OCV), the current or the impedance, so as to estimate the SOH. Measuring the OCV directly is to estimate the SOH through the intrinsic relationship between the OCV curve and capacity [8], while measuring the current directly to estimate the SOH is achieved by integrating the current flowing into or out of the battery [9]. On the other hand, measuring the impedance directly is to estimate the SOH considering the principle that the more serious the battery aging, the greater internal resistance at low frequency [10]. Electrochemical impedance spectroscopy (EIS) is the most commonly used method. The relationship between EIS and the SOH can be obtained by nondestructive measurement of the LIB impedance [11]. In addition to the EIS method, current pulse and the Joule effect are also used to measure the internal resistance [12, 13]. Although the direct measurement method has high accuracy and low

*Correspondence: wkwj888@163.com

[1] School of Electrical Engineering, Weihai Innovation Research Institute, Qingdao University, Qingdao 266000, China
Full list of author information is available at the end of the article

computational complexity, it needs additional hardware and the precision instruments needed for accurate measurement are expensive. Thus, this method is more suitable for the laboratory environment and conditions, and it is difficult to realize online estimation.

The model-based methods include the electrochemical, empirical degradation and equivalent circuit models. The electrochemical model is to study the aging of the LIB from the internal chemical working mechanism, such as internal lithium-ion diffusion, average radius of solid particles, and changes of negative electrode materials [14, 15]. The accuracy of this method can meet the requirements, but the establishment of the electrochemical model is too complicated and many partial differential equations need to be set up. At the same time, the established model is too targeted and can only estimate the aging process of a specific type of battery or under specific conditions, so it is not suitable for practical application. Empirical degradation models find it easy to identify parameters and have good robustness, and can be applied online [16]. However, the battery capacity will fluctuate locally in the whole life cycle of a LIB, and this cannot be reflected in the empirical degradation models [17]. The equivalent circuit model is obtained by simulating the working state of the battery through circuit elements [18, 19]. The method estimates the SOH by identifying the model parameters. After modeling, Kalman filter and other methods are usually used to achieve parameter fitting [20, 21]. In [22], a second-order RC equivalent circuit model is established and the adaptive unscented Kalman filter algorithm is used to estimate the ohmic internal resistance of the battery in real time. The SOH is then estimated according to its mapping relationship with the ohmic internal resistance. This model has the advantages of being intuitive, of general and simple structure, while the relationship between voltage, current and impedance can be analyzed through circuit diagrams. However, the adaptability is poor, and the model parameters are difficult to accurately identify. Factors such as current, discharge power, charge rate and temperature have nonlinear effects on battery characteristics, and these are difficult to take into account when modeling. At the same time, the internal parameters of the battery change with time, and this cannot be reflected in the equivalent model, and thus the model cannot respond well to a fluctuation of capacity [23].

In recent times the data acquisition and calculation have greatly improved, so the data-driven methods are very popular and have been widely used in various classifications and estimates [24–29]. Compared with other methods, the data-based methods do not need to deeply understand the internal mechanism of the battery. They analyze the external characteristics closely related to battery aging, such as voltage, current, battery temperature, etc. Through the data-driven methods, the nonlinear mapping relationship between these parameters or parameter deformation and battery capacity can be established, thus avoiding the complicated process of chemical analysis and parameter identification [30]. The main data-driven methods include linear regression, support vector machine and neural networks, etc. For example, in [31], logistic regression and regularization are used to estimate the cycle life of the battery, although the accuracy needs to be improved, and the estimation error is 9.1%. In [32, 33], the estimation method using the improved ant colony optimization algorithm to optimize the support vector regression, and the estimation model based on the bidirectional long-term memory neural network, are proposed, respectively. Although the estimation accuracy is improved, the generalizability of each model is low, and the cycle times of SOH estimation in each battery data set are insufficient. Generally speaking, the extracted features are critical to the application of data-driven methods in practice. In [34], the terminal voltage during discharge is used as an input to the model, and Box-Cox transformation is used to improve the correlation between the input and battery capacity. However, it is unrealistic to use the data in the discharge process to realize the estimation, because the data in that process is unstable while the voltage or current vary according to the load. In addition, the incremental capacity (IC) curve is used for extracting new features. In [35], a construction method is used to reshape the IC curve and new features with high correlation rate are extracted from the modified IC curve. In [36], joint gray-scale correlation analysis is used to extract the optimal local IC curve for new features. However, when using the IC curve to realize SOH estimation, it is necessary to extract the IC curve first. Thus, if the deformation of the IC curve is used, a new step is needed to extract the features. These are not conducive to applying the model in practice. Therefore, the features based on the IC curve are not the most direct and effective, and it is most beneficial for practical application to extract the features directly from voltage or current.

The data-driven methods are efficient ways to estimate the SOH, and have strong adaptability to nonlinear systems. Looking back at the current data-driven SOH estimation methods, although there are many types and their development has been rapid, these methods still have the following problems:

1. The existing data-driven methods rarely consider the noise in the battery data. Because of the influence of the running state and environment, information

collected by the data sensor always has noise, so the extracted features also contain wrong information.
2. The features extracted by existing estimation methods are not always the most straightforward and effective in a particular context and application. Some have poor estimation effect, because of either using unstable discharge data, or extracting features requiring complex processing which adds extra computation.
3. The current SOH estimation methods only consider the existing experimental data, so the model will not be updated after training. For the complex situation of actual estimation, the training samples are obviously insufficient, and this makes the model lack generalizability and be unable to update experimental data.
4. Both high and low temperatures have important effects on the SOH of LIBs [37, 38]. However, the existing methods only validate the performance of the model at 24 °C without considering the effect of temperature.
5. When the parameters of data-driven models are trained, there will be local optimization problems and even gradient explosions.

In solving the above problems, the main contributions of this paper are summarized as follows:

1. Combining the MAD filtering with SG filtering, a MAD-SG filtering method is proposed to process the data. Using MAD-SG improves the correlation rate between the proposed features and the capacity of the LIB without making it excessively smooth, so the estimated SOH can still reflect the local recovery of capacity.
2. For analyzing the aging of LIB, five features are proposed. The advantages of these features are that the correlation rates are greater than 0.99 after MAD-SG filtering, and only the voltage and current in the charging stage are needed. In addition, compared with existing features, the features proposed in this paper require no complicated processing nor calculation.
3. Adding the IUM of battery data. The data obtained after each estimation is added to the training set to make full use of the battery data to improve the generalizability of the model.
4. Considering the influence of temperature, the generalizability of the model is further verified by the data of the low-temperature and high-temperature battery.
5. The SSA-Elman model is proposed for the first time. A novel SSA optimization algorithm is used to optimize the weights and thresholds of the Elman neural network, and this can prevent local optimization problems and improve calculation accuracy.

The rest of the paper is organized as follows: Sect. 2 introduces the data processing method and feature extraction process, while Sect. 3 describes the general framework of the proposed method, the SSA-Elman model and the IUM. In Sect. 4, the SSA-Elman model and proposed features are verified by experiments, and the experimental results are given. Finally, conclusions are presented in Sect. 5.

2 Extract features

2.1 SOH definition

The basic definition of SOH is the ratio between the current and nominal capacities, as:

$$SOH = \frac{C_P}{C_N} \times 100\% \tag{1}$$

where C_P is the current actual capacity and C_N is the nominal capacity [39]. In the course of the operation of the battery, its SOH decreases continuously.

2.2 Data sources

The dataset from the NASA Ames prognostics center of excellence (PCoE), i.e., BatteryAgingARC-FY08Q4, BatteryAgingARC_25-44 and BatteryAgingARC_45-48, is used in the experiments. The analysis process for extracting features uses B0005, B0006, B0007, and B0018 in the dataset. In addition to the four batteries, B0046, B0047, and B0048 in the BatteryAgingARC_45-48 dataset and B0029, B0030, and B0031 in the BatteryAgingARC_25-44 dataset are also used in the experimental verification process [40]. All batteries are commercial 18650 LIB, and the data type is the mat format of MATLAB.

The experimental process is repeated charging and discharging until the nominal capacity drops by around 30%. Charging is performed under constant current (CC)–constant voltage (CV) mode and discharging is under CC mode. Figure 1 shows the charging and discharging voltage and current of B0005, where Fig. 1a and b show the terminal voltage and current during charging and discharging, respectively. As shown in Fig. 1a, the battery is charged in CC mode of 1.5 A until its terminal voltage reaches 4.2 V, and then it is charged in CV mode until the charging current drops to 20 mA. In Fig. 1b, discharging is performed in CC mode at 2 A until the battery terminal voltage drops to 2.7 V. The operation of the selected battery dataset during charging is the same, but the differences are the experimental temperature, the discharging current and the cut-off voltage during discharging. The details of each battery dataset are shown in Table 1.

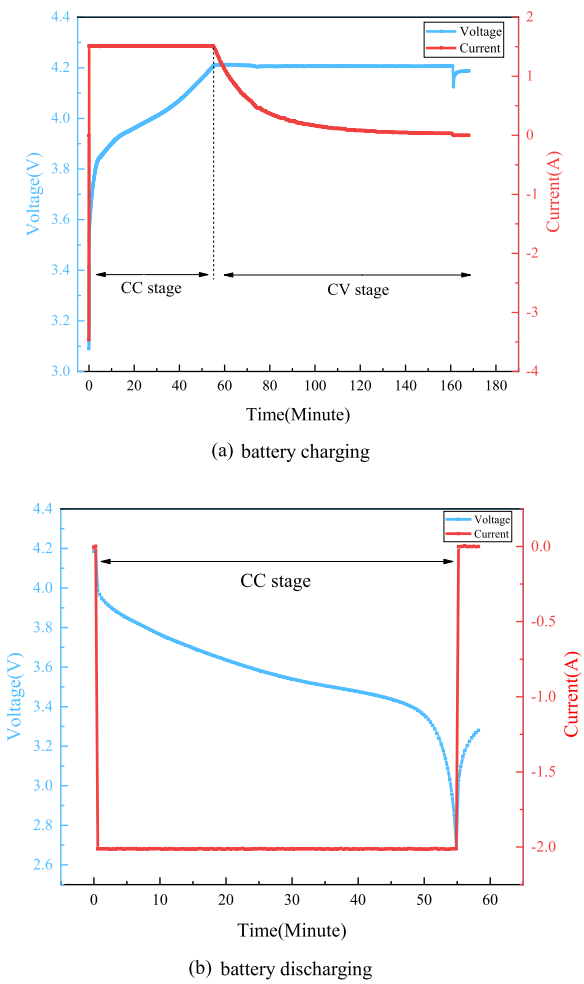

Fig. 1 Terminal voltage and terminal current for charging and discharge of B0005

2.3 Aging mechanism of LIB

A fundamental issue to consider when using LIBs is the aging of the batteries. Figure 2 shows the decreasing capacity of four LIBs with the number of cycles. LIB aging is a very complex process, and is caused by physical and chemical mechanisms. It can be seen in Fig. 2 that this decline is not a simple linear one, and there are some small increases in capacity during the aging [41], which are due to charges stored in the region of the negative electrode that extend beyond the positive electrode [42, 43]. Such capacity fluctuations cannot be ignored when estimating the SOH.

Figure 3 shows the aging mechanism of LIBs. This is mainly caused by the loss of lithium-ion inventory and the loss of active species [44]. The aging of LIBs is that the actual capacity declines and the internal resistance increases [45], as lithium-ion deposits to form a solid electrolyte interface (SEI) layer on the surface of the negative electrode. This hinders the insertion and detachment of the lithium-ion. The SEI layer is the result of side electrochemical reactions when lithium-ions are consumed. The increase of the internal resistance will accelerate the terminal voltage reaching the upper cut-off voltage limit to a certain extent during charging, thus reducing rechargeable power. With the increase of charging and discharging cycles, chemical reactions occur repeatedly inside the battery and the performance of the LIB decreases gradually.

2.4 Data processing method

There will inevitably be outliers and noise in the data collected in the experiments. In order to eliminate the influence of outliers and noise, it is necessary to preprocess

Table 1 Details of the selected dataset

Data set		Temperature (°C)	Discharge (A)	Cut-off voltage (V)	Size (MB)
BatteryAgingARC-FY08Q4	B0005	24	2	2.7	15.2
	B0006	24	2	2.5	15.2
	B0007	24	2	2.2	15.3
	B0018	24	2	2.5	8.10
BatteryAgingARC_25-44	B0029	43	4	2.0	2.74
	B0030	43	4	2.2	2.74
	B0031	43	4	2.5	2.74
BatteryAgingARC_45-48	B0046	4	1	2.2	3.47
	B0047	4	1	2.5	3.54
	B0048	4	1	2.7	3.57

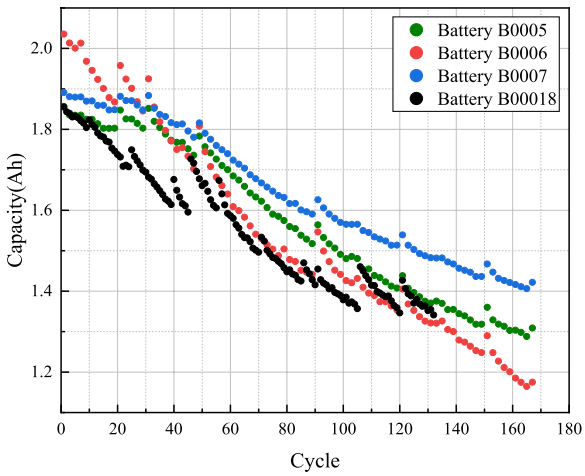

Fig. 2 Capacity curve of LIB with the number of cycles (B0005, B0006, B0007 and B0018)

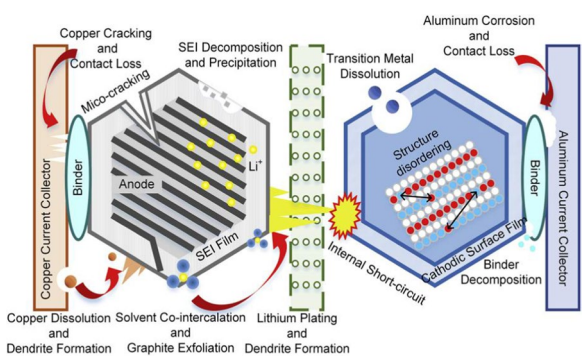

Fig. 3 Aging mechanism of lithium battery. Reprinted with permission from [46]. Copyright 2016, Elsevier B.V

the data so as to improve the correlation rate between features and capacity of the LIB. In this paper, MAD and SG filtering are combined to form the MAD-SG filtering method.

The general idea is to specify a threshold of data fluctuation, and when the data exceeds the threshold, it is considered as an abnormal value [47]. The principle is as follows.

Set the window size as m, and $X_{m\times 1}$ represents all the data contained in the window. The median of $X_{m\times 1}$ is calculated first, and the absolute deviation between each data point and the median of $X_{m\times 1}$ is then calculated as:

$$MAD = median\left(\left|x_i - median(X_{m\times 1})\right|\right) \tag{2}$$

Generally, the threshold is an integer multiple of MAD. When there are data points that exceed this threshold, the data is considered as an outlier.

SG is a smoothing filter based on polynomial fitting to eliminate noise and minimize the error of mean-square of $2M+1$ samples centered on $n=0$. This method can better retain the distribution characteristics of relative maximum, minimum and width [48]. Its principle is to obtain the best coefficients of the polynomial in the following equation:

$$y(n) = \sum_{i=0}^{N} a_i n^i \tag{3}$$

where $y(n)$ represents the coefficients of the polynomial, a_i represents the coefficient of each value and n^i represent the counter of the effective data on the smoothed value.

The optimal coefficients will result in minimized error in $2M+1$ samples, while the error function is shown as:

$$\begin{aligned} \in_N &= \sum_{n=-M}^{M} \left(y(n) - x[n]\right)^2 \\ &= \sum_{n=-M}^{M} \left(\sum_{i=0}^{N} a_k n^k - x[n]\right)^2 \end{aligned} \tag{4}$$

where $\in_N$ is the error function for the Nth polynomial and $x[n]$ is the raw value of the nth data.

By setting the derivative of the error function to 0, the optimal coefficient can be obtained, as:

$$\frac{\partial \in_n}{\partial a_i} = 0 \tag{5}$$

Finally, the filtered data can be obtained by putting the best coefficient into (3).

Given the fluctuation of data, for the MAD method, this paper selects three times the M of every 10 points as the threshold for outlier processing. The eliminated outliers are replaced with the linear interpolation of adjacent values. For SG filtering, after testing, the effect is best when $M=2$ and $k=3$. When processing the data, the MAD filter is first used to remove the outliers, and then the SG filter is used for smoothing. The MAD-SG filter can well retain the characteristics of local recovery of capacity, remove the outliers and smooth the data. After data processing, the correlation rates between features and LIB capacity have improved. The effect of MAD-SG is shown in Table 3 and Fig. 5 in Sect. 2.5.

2.5 Propose features

Using data-driven method to realize the estimation of SOH is mainly to find the features which have high a correlation rate with the SOH. In real application, the

charging process of the LIB is under CC–CV mode, which is consistent with different types of LIBs. However, the discharging process varies with the actual load, and it is difficult to extract stable features. Therefore, this paper only uses the data of the charging stage to extract features.

The Pearson correlation coefficient is widely used as an important index to measure the correlation rate between two vectors. The calculation formula of Pearson correlation is given as:

$$P_{X,Y} = \frac{Cov(X,Y)}{\sigma X \sigma Y} \tag{6}$$

where X and Y are two vectors, $Cov(X,Y)$ is the covariance of X and Y, while σX and σY are the standard deviations of X and Y, respectively. The value of the Pearson correlation is between -1 and 1. If it is greater than 0, the two vectors are positively correlated, and if it is less than 0, the two vectors are negatively correlated. If the correlation rate is 0, the two vectors are irrelevant. Greater $|P_{X,Y}|$ means higher correlation rate, while the higher the correlation rate, the better the accuracy of estimating Y with X.

Figure 4 shows the relationship between the terminal voltage and charged electric quantity (CEQ) of B0005 during the CC charging stage, referred to as a V–Q curve. V represents the terminal voltage of the battery, which is measured directly by the sensor, and Q represents the charged electric quantity, which is obtained by integrating the charging current. In Fig. 4, as the number of cycles increases and the battery ages, the V–Q curve begins to move up and left gradually. Because the impedance of the LIB increases, the LIB reaches the upper limit of the cut-off voltage faster.

In addition, it can be seen from Fig. 4 that in the CC charging stage, as the battery cycle increases, the battery aging becomes more serious, and less electrical quantity is charged when the voltage reaches 4.2 V. Based on this phenomenon, a correlation rate analysis of the CEQ and LIB capacities in different voltage ranges can be performed.

Before analysis, the MAD-SG filter is used to process all data. Figure 5 shows the curves of CEQ when the terminal voltage reaches 4.2 V after processing the data with different filtering methods. As seen in Fig. 5, there are two obvious outliers. The small fluctuation of the curve is the embodiment of the capacity recovery phenomenon. It can be seen that MAD cannot fit the original curve well although it removes the outliers. In contrast, SG can fit the original curve well but retains the outliers, while MAD-SG removes the outliers and can also fit the original curve well.

The results of correlation rate are shown in Table 2. It can be seen that the CEQ in the CC charging stage has high correlation with the LIB capacity. The first feature proposed is called CEQ1 for voltage from 3.4 to 4.2 V, and the Pearson correlation coefficient between CEQ1 and LIB capacity is 0.9975. The second feature proposed is called CEQ2 for voltage from 3.8 to 4.2 V in the CC charging stage, and the correlation between CEQ2 and the LIB capacity is 0.9958.

In Fig. 4, the V–Q curve of the aged battery shifts to the upper left compared with the new battery, so the areas contained in the integration of V to Q are also different. Therefore, the next feature proposed is the area contained in the integral of V to Q within the specified voltage range, i.e., the V–Q area (VQA). The correlation rate between the VQA of voltage range selected and battery capacity is also different according to start voltage and end voltage, as shown in Table 3.

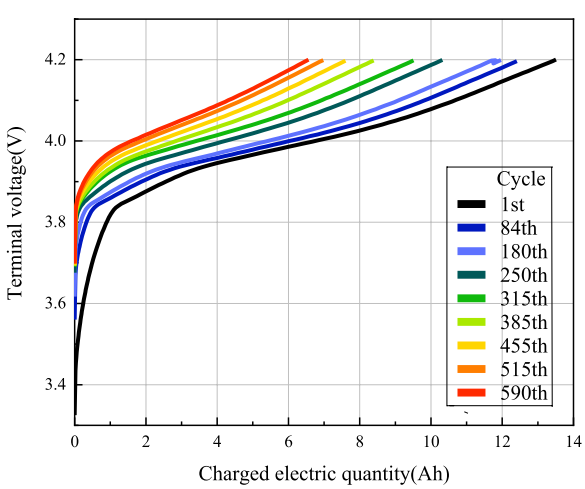

Fig. 4 V–Q curve of B0005 battery

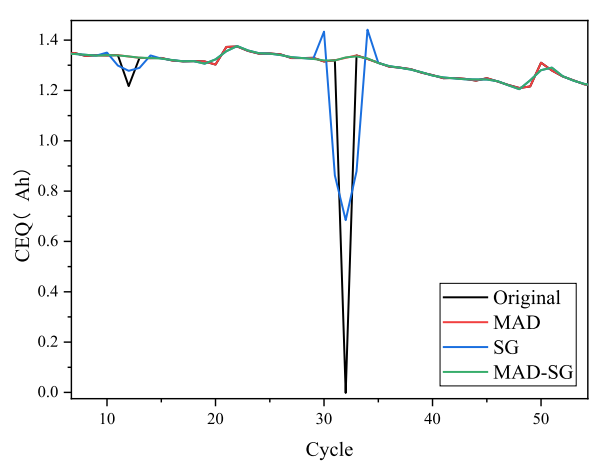

Fig. 5 The curve of CEQ when the terminal voltage reaches 4.2 V after processing the data with different filtering methods

Table 2 Pearson correlation analysis between CEQ and LIB capacity with different voltage ranges

START	END						
	3.6 V	**3.7 V**	**3.8 V**	**3.9 V**	**4.0 V**	**4.1 V**	**4.2 V**
3.3 V	0.6589	0.7007	0.8326	0.9617	0.9928	0.9966	0.9975
3.4 V	0.6589	0.7007	0.8326	0.9617	0.9928	0.9966	0.9975
3.5 V	0.6764	0.7063	0.8358	0.9626	0.9929	0.9966	0.9975
3.6 V		0.7469	0.8566	0.9687	0.9936	0.9968	0.9974
3.7 V			0.8956	0.9788	0.9945	0.9967	0.9970
3.8 V				0.9884	0.9952	0.9961	0.9958
3.9 V					0.9941	0.9932	0.9916
4.0 V						0.9778	0.9688
4.1 V							0.9406

Table 3 VQA correlation analysis of different voltage intervals

Start	End								
	3.4 V	**3.5 V**	**3.6 V**	**3.7 V**	**3.8 V**	**3.9 V**	**4.0 V**	**4.1 V**	**4.2 V**
3.3 V	−0.8669	−0.7329	−0.6854	−0.6870	−0.7467	−0.8615	−0.7188	−0.9825	−0.9493
3.4 V		−0.4920	−0.5103	−0.5616	−0.6652	−0.8120	−0.7127	−0.9772	−0.9572
3.5 V			−0.6182	−0.6560	−0.6923	−0.7232	−0.4458	−0.9690	−0.9824
3.6 V				−0.6734	−0.7241	−0.2432	−0.4247	−0.9192	−0.8123
3.7 V					0.6827	0.4091	0.4032	0.3221	−0.0319
3.8 V						−0.8447	0.5349	−0.7866	0.2480
3.9 V							0.7675	0.8415	0.9710
4.0 V								0.6962	0.9739
4.1 V									−0.4755

It can be seen from Table 3 that before the start voltage reaches 3.7 V, the correlation is negative regardless of the end voltage, whereas the positive correlation begins to appear after the start voltage reaches 3.7 V. The maximum negative correlation is −0.9825, and the interval is 3.3–4.1 V. The maximum positive correlation is 0.9739, and the interval is 4.0–4.2 V. In order to express the relationship between the selected interval and the coefficient more intuitively, the data in Table 3 are drawn into a three-dimensional surface graph and a profile analysis diagram using the interpolation method, as shown in Figs. 6 and 7, respectively.

By trying the intervals with high correlation rate in the three-dimensional surface diagram, the interval with higher correlation rate than that in Table 2 is finally obtained. The area of interval 3.305–4.175 V is taken as the third feature VQA3, and its correlation is −0.9925. The area of interval 3.425–4.179 V is taken as the fourth feature VQA4, and the correlation is −0.9915.

To calculate the CEQ, the charging time needs to be recorded. In order to improve the utilization of data,

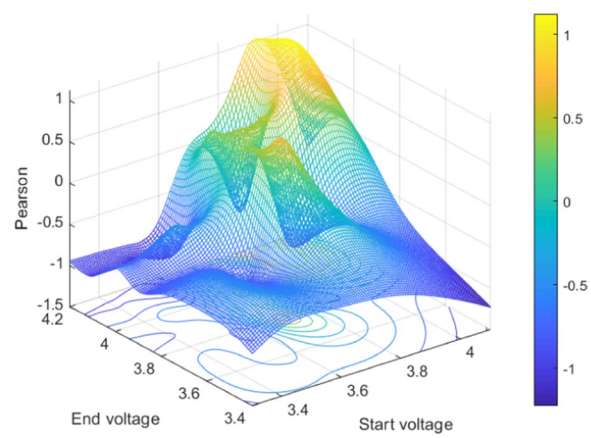

Fig. 6 Three-dimensional surface diagram of start voltage, end voltage and Pearson correlation rate

the fifth feature is extracted based on the charging time. However, considering that users do not fully charge every time in practical application, the total charging time is optimized. Thus, the fifth feature is the time from the

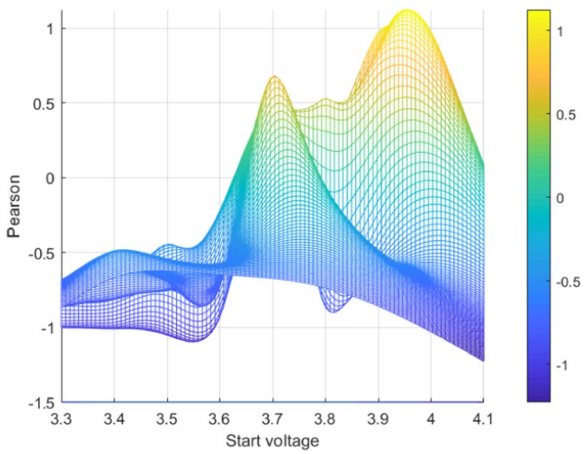

Fig. 7 Profile analysis diagram of three-dimensional surface diagram

beginning of charging to the battery terminal current falling to 0.8 A, which is called partial charging time (PCT5). The correlation between PCT5 and LIB capacity is 0.9972.

The features are proposed from the two dimensions of voltage and current, which can only be extracted by collecting the charging data, while corresponding to different stages of the charging process. This is to better fit the actual working conditions of the battery, so that some features can be extracted even when the battery is not fully charged and discharged. Finally, the correlation rates between the five features and LIB capacity are shown in Table 4. At the same time, Table 4 also gives the correlations after different processing. It can be seen from Table 4 that the correlations obtained after using

Table 4 Pearson correlation rates between the five features and capacity of B0005 battery

Features	CEQ1	CEQ2	VQA3	VQA4	PCT5
Unprocessed	0.8743	0.8732	−0.9097	−0.8974	0.6658
MAD	0.9651	0.9598	−0.9302	−0.9272	0.9317
SG	0.9423	0.9319	−0.9648	−0.9579	0.9682
MAD-SG	−0.9925	−0.9915	0.9975	0.9974	0.9972

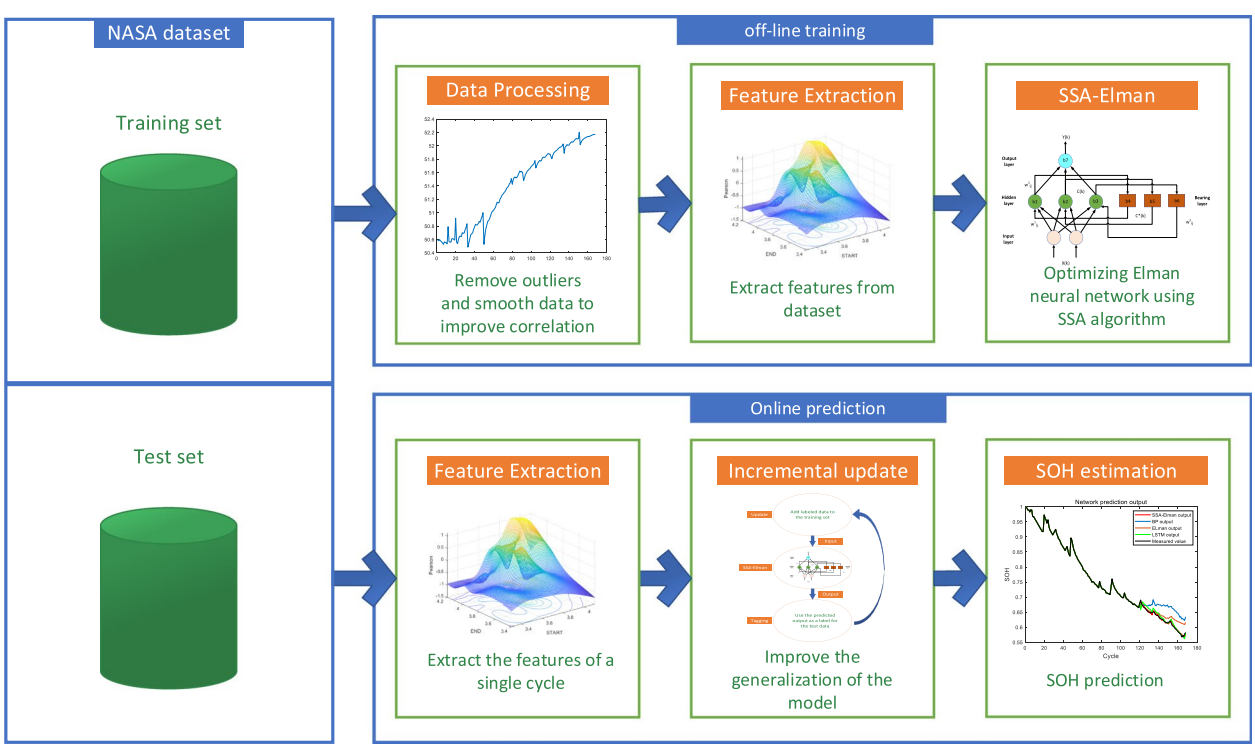

Fig. 8 Model structure

the MAD-SG processing are the highest, with all above 0.99.

3 Proposed model

3.1 Overall framework

In this paper, SSA is used to optimize an Elman neural network so as to realize accurate estimation of SOH. The specific model structure is shown in Fig. 8. The scheme can be divided into two parts: off-line training model and on-line SOH estimation. The off-line part is mainly to process data, extract features and train the SSA-Elman model. During the experiments, the discharge capacity given by the NASA dataset is used as the reference value. Based on the off-line training part, the online estimation part uses the SSA-Elman model trained for estimation. To further improve the performance of the model, the incremental update mechanism (IUM) is added. The voltage and current are input for only one cycle per estimate, while after the estimation, the output of the model is used as the label for the input of this cycle to update the data. This process repeats until the end of estimation. Finally, the online estimation of SOH for LIB is realized.

3.2 Elman neural network

The Elman neural network is a fully-connected dynamic feedback neural network, which has a local memory unit and local feedback function. It can not only realize the modeling of a static system, but also realize the mapping of a dynamic system and directly reflect the dynamic characteristics of the system [49]. Compared with a feedforward neural network, Elman adds an additional receiving layer on the basis of the three-layer structure of input, hidden and output layers, and is a one-step delay operator, which achieves the purpose of short-term memory. Therefore, the Elman model has the ability to adapt to time-varying characteristics. At the same time, it has stronger computing power and network stability [50]. While there is a nonlinear relationship between the parameters of LIB and SOH, these characteristics of the Elman neural network enable it to approach any nonlinear relationship with ideal accuracy. Therefore, the Elman neural network is chosen as the infrastructure in this paper.

Figure 9 shows the Elman neural network structure with two input units, three hidden units and one output unit [51]. In Fig. 9, k represents the kth time, $X(k)$ represents the input vector of the input layer, $w_{i,j}^1$, $w_{i,j}^2$ and $w_{i,j}^3$ represent the connection weights from the input layer to the hidden layer, from the receiving layer to the hidden layer, and from the hidden layer to the output layer, respectively. $C(k)$, $C^*(k)$ and $Y(k)$ represent the output vectors of the hidden, receiving, and output layers, respectively. $b1$ to $b4$ are the thresholds of the receiving and output layers, respectively. The mathematical expressions of the network are:

$$C^*(k) = C(k-1) \tag{7}$$

$$C(k) = f\left(w_{i,j}^1 X(k) + bi + w_{i,j}^2 C^*(k)\right) \tag{8}$$

$$Y(k) = g\left(w_{i,j}^3 C(k) + bi\right) f(\cdot) \tag{9}$$

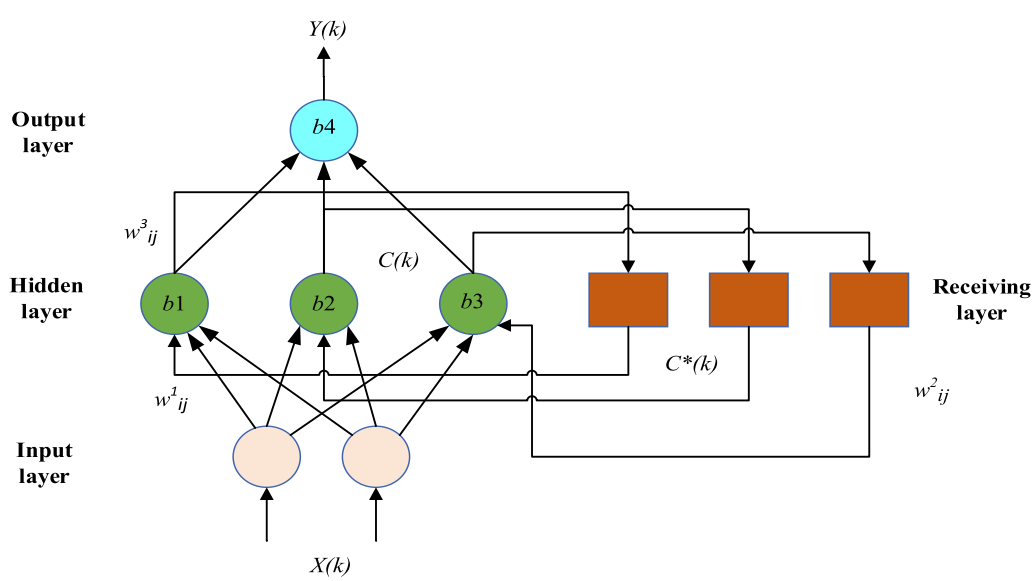

Fig. 9 Elman neural network structure with two input units, three hidden units and one output unit

where bi represents the corresponding threshold, $g(\cdot)$ represents the activation function of output neurons, which is generally a linear combination, and $f(\cdot)$ represents the activation function of the hidden layer.

However, Elman also has the inherent defects of a neural network [52], such as slow training speed and easy to fall into local minima. These affect the training efficiency and estimation accuracy. In order to solve the problems, SSA is used to optimize the connection weight and threshold of Elman neural network, which can prevent it from falling into a local minimum and improve the training speed and estimation accuracy.

3.3 Sparrow search algorithm

The SSA is a new type of natural heuristic algorithm based on group socialization characteristics. It was proposed according to the behavior of sparrows foraging and avoiding predators. The algorithm has the advantages of simple structure, easy implementation, few control parameters, strong optimization ability etc. The way for SSA to converge to the current optimal solution is to jump directly to the vicinity of the current optimal solution, so the SSA algorithm is superior to the grey wolf optimization, gravity search and particle swarm optimization algorithms in terms of accuracy, convergence speed, stability and robustness [53, 54].

In the SSA algorithm, sparrows are divided into discoverer, follower and vigilant. The position of each sparrow corresponds to a solution. The positions of all sparrows in the sparrow group are represented by the X matrix, as:

$$X = \begin{pmatrix} x_{1,2} & \cdots & a_{1,d} \\ \vdots & \cdots & \vdots \\ x_{m,1} & \cdots & x_{m,d} \end{pmatrix} \tag{10}$$

where m represents the number of sparrows, and d represents the dimension of the variables to be optimized.

The fitness function corresponding to each sparrow is represented by the F matrix, as:

$$F = \begin{pmatrix} f([x_{1,1} & \cdots & x_{1,d}]) \\ \vdots & \cdots & \vdots \\ f([x_{m,1} & \cdots & x_{m,d}]) \end{pmatrix} \tag{11}$$

where $f([x_{i,1}, \cdots, x_{i,d}])$ in line i represents the fitness value of the ith sparrow. At each iteration, the location of the discoverer will be updated, as:

$$X_{i,j}^{t+1} = \begin{cases} x_{i,j}^{t} \cdot \exp\left(\frac{-i}{\alpha \cdot N}\right), & if\ R_2 < ST \\ x_{i,j}^{t} + Q \cdot L, & if\ R_2 \geq ST \end{cases} \tag{12}$$

where t represents the current number of the iteration, and N represents the maximum number of iterations. α is a random number and $\alpha \in (0, 1]$. R_2 represents the alarm value, which is a random number and $R_2 \in [0, 1][0, 1]$. ST represents the safety threshold and $ST \in [0.5, 1.0]$. Q is a random number subject to a normal distribution, and L is a row vector whose elements are all equal to 1.

The update rule of the follower is given as:

$$X_{i,j}^{t+1} = \begin{cases} Q \cdot \exp\left(\frac{X_W^t - X_{i,j}^t}{i^2}\right), & if\ i > \frac{n}{2} \\ x_{DB}^{t+1} + |X_{i,j}^t - x_{DB}^{t+1}| \cdot M' \cdot L, & if\ i \leq \frac{n}{2} \end{cases} \tag{13}$$

where X_W^t represents the worst position of the tth iteration, and x_{DB}^{t+1} represents the position of the finder with the highest fitness value at iteration t+1. M represents the $1 \times d$ matrix, in which the elements are randomly preset as 1 or -1. $M' = M^T(M \cdot M^T)^{-1}$, and M^T means the matrix is transposed.

The location update of the vigilant is:

$$X_{i,j}^{t+1} = \begin{cases} x_{GB}^{t} + \gamma \cdot |X_{i,j}^t - x_{GB}^t|, & if\ f_i \neq f_B \\ x_{GB}^{t} + k \cdot \left(\frac{X_{i,j}^t - x_{GB}^t}{|f_i - f_w| + \varepsilon}\right), & if\ f_i = f_B \end{cases} \tag{14}$$

where x_{GB}^t represents the globally optimal location in the tth iteration, γ is the control step size and $\gamma - N(0, 1)$. k is a random number and $k \in [-1, 1]$, while ε is a constant that increases to prevent the denominator from being 0. f_i is the fitness value of the ith sparrow, while f_B and f_w represent the global optimal and worst sparrow fitness values, respectively.

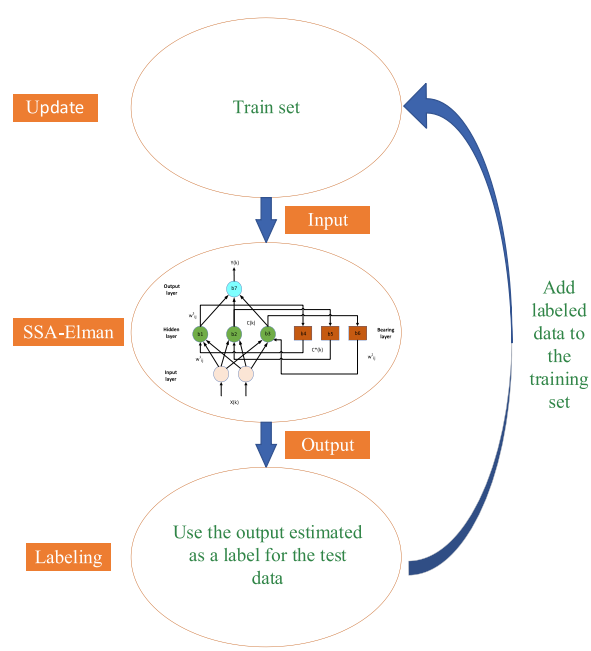

Fig. 10 The IUM principle

Table 5 The parameters of Elman neural network

Network	Input layers	Hidden layers	Output layers	Epochs	Learning rate
Elman	5	15	1	500	0.0001
LSTM	5	50	1	500	0.005

The super parameters that the SSA algorithm can adjust include the maximum number of iterations N, the number of sparrows n and the safety value ST. In addition, there are the number of discoverers PD, the number of vigilantes SD, and the upper and lower limits of the independent variable DL. The dimension d of the independent variable is jointly determined by the input vector and the number of network layers.

3.4 Incremental update mechanism

The generalizability of the model determines whether the model can be applied in practice. This is closely related to the amount of training data. Therefore, the IUM is added to improve the generalizability of the model. The mechanism is shown in Fig. 10. First, the SSA-Elman model is trained with the processed training set, and an estimate is then made, while only one cycle of SOH needs to be estimated for each estimation. Next, the estimated output is used as the label of the input, i.e., labeling. Finally, the labeled data is added to the training set, and the SSA-Elman model is updated. Therefore, the dataset and the SSA-Elman can be dynamically updated based on new data. Using the IUM can not only make full use of battery data, but also improve the generalizability of the model.

4 Experimental verification

4.1 Validation process

The experiments are implemented with MATLAB R2020B programming on a laptop. In the experiments, the data of B0005, B0006, B0007 and B0018 are selected to verify the accuracy and generalizability of the proposed method. First, 70% of the data is used for training, and the rest is used to test the basic performance of the model. The model is then trained using 50% and 30% of the data to test the generalizability and robustness of the model. Finally, in order to further verify the performance of the model, the model is used for SOH estimation of a LIB at low and high temperatures, respectively. Both high-temperature and low-temperature experiments included three batteries. Two batteries in each experiment are used as the training sets and the third is used as the test set. To reflect the performance of the model more clearly, the method is compared with the basic Elman neural network and the LSTM neural network. In the experiments, RMSE and MAPE are selected as the evaluation criteria of the model, calculated as:

$$RMSE = \sqrt{\frac{1}{n}\sum_{i=1}^{n}\left(\tilde{y}_i - y_i\right)^2} \tag{15}$$

$$MAPE = \frac{100\%}{n}\sum_{i=1}^{n}\left|\frac{\tilde{y}_i - y_i}{y_i}\right| \tag{16}$$

where n represents the total number of cycles, $\tilde{y}_i$ and y_i represent the predicted and measured values of the ith cycle, respectively. To prevent chance, the RMSE and MAPE given next are the average RMSE and MAPE obtained by running the model 5 consecutive times.

4.2 Model parameters

The inputs are the five features proposed in Sect. 2, so there are five dimensions to the inputs. The parameters of the Elman and the LSTM are shown in Table 5. The super parameters that can be adjusted in the SSA algorithm mentioned in Sect. 3, such as the maximum number of iterations N and population size n, the number of discoverers PD, the number of vigilantes SD, the safety value ST, the upper and lower limits of the independent variable DL, and the dimension of the parameters to be optimized d, are set as shown in Table 6. RMSE is used as the fitness function to optimize the Elman neural network.

Figure 11 shows the curves of fitness value changing with the number of iterations. As shown, the fitness values gradually decrease during the iteration, which indicates that the SSA algorithm has found suitable network parameters. In addition, the optimization of the parameters is completed before 20 iterations, which proves that the SSA is fast and effective.

4.3 Results analysis

Figure 12 shows the outputs of the SSA-Elman, Elman and LSTM when using 70% training data. The output of the SSA-Elman model is clearly closer to the measured value than the Elman model. The output of the LSTM model is also ideal, but individual points deviate from the measured values, while the SSA-Elman model does not have such fluctuations. The accuracy of the SSA-Elman

Table 6 The super parameters that can be adjusted in the SSA algorithm

Parameters	*N*	*n*	*PD*	*SD*	*ST*	*DL*	*d*
Setting	100	50	0.7	0.2	0.6	[− 5,5]	121

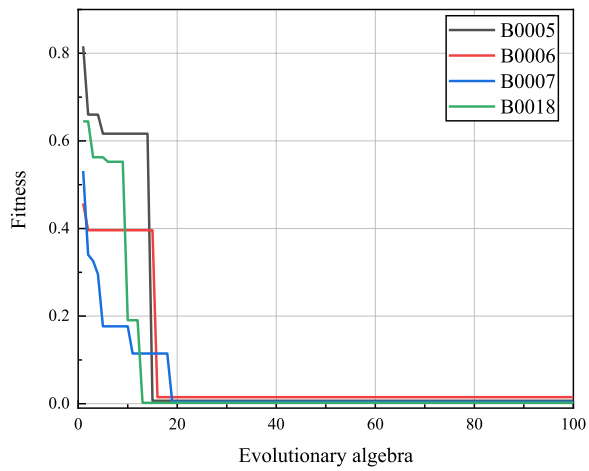

Fig. 11 The curve of fitness value changing with the number of iterations

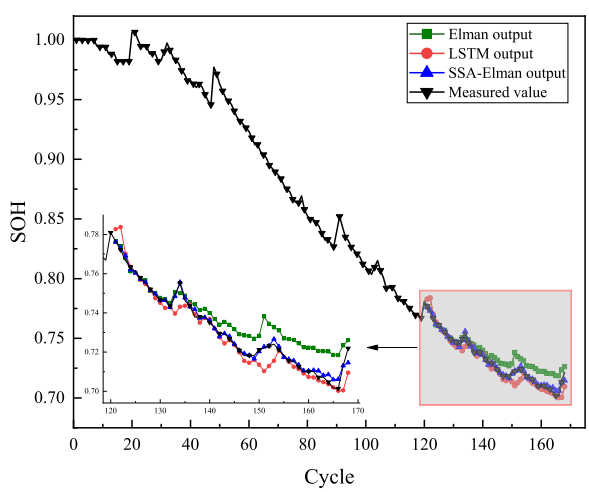

Fig. 12 The outputs of SSA-Elman, Elman and LSTM when using 70% training data

model is significantly higher than the Elman neural network and LSTM neural network. The specific estimation errors with 70% training data are shown in Table 7.

It can be clearly seen in Table 7 that the estimation error of SSA-Elman is the lowest of the networks, with the lowest RMSE of 0.0024 and the lowest MAPE of 0.14%. Using the SSA to optimize the Elman neural network reduces RMSE by at least 0.0061 and MAPE by at least 0.67%. In Table 7, the errors of B0006 and B0018 are larger, because the capacities of these two batteries fluctuate greatly. Compared with Elman and LSTM, SSA-Elman is more adaptable to the fluctuations so the corresponding errors are smaller. This is because the network parameters optimized by the SSA algorithm are more suitable for the fluctuation of capacity. It can be seen that using the SSA algorithm to optimize Elman has achieved good results, and the accuracy and stability of the SSA-Elman model can meet the requirements.

4.4 Verification of generalization

The generalizability of the model is very important, so further verifications are carried out. Here, 50% data and 30% data are used to train the model to verify the generalizability of the SSA-Elman model. Figure 13 shows the outputs of Elman, LSTM and SSA-Elman when using 50% training data. As can be seen from Fig. 13, the errors of the networks increase after reducing the training data, but the errors of SSA-Elman are significantly smaller than those of the other networks. When the training data is only 50%, Elman and LSTM can still maintain the same downward trend as the measured value, but the deviations of the curves become obvious. It is worth pointing out that the SSA-Elman model can still show good estimation ability, because of the added IUM to the SSA-Elman model, which improves the generalizability of the model.

Table 7 The estimation error of 70% training data RMSE and MAPE

Method	B0005		B0006		B0007		B0018	
	RMSE	MAPE (%)	RMSE	MAPE (%)	RMSE	MAPE (%)	RMSE	MAPE (%)
Elman	0.0085	0.94	0.0210	2.15	0.0088	0.96	0.0168	1.76
LSTM	0.0051	0.49	0.0094	0.91	0.0053	0.51	0.0082	0.79
SSA-Elman	0.0024	0.27	0.0054	0.42	0.0026	0.25	0.0053	0.51

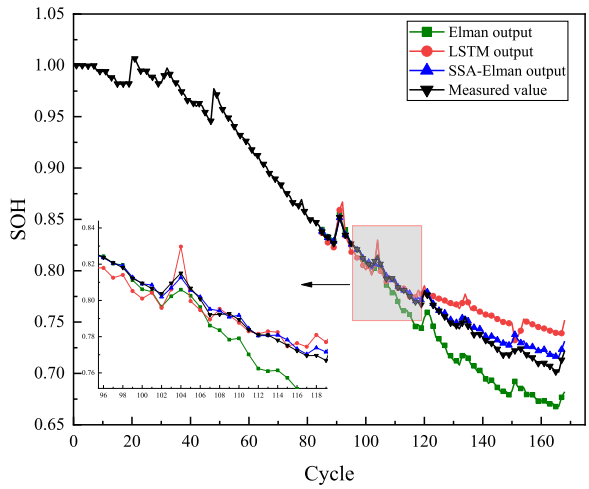

Fig. 13 The outputs of SSA-Elman, BP, Elman and LSTM when using 50% training data

Table 8 shows the estimated errors of Elman, LSTM and SSA-Elman when using 50% of the training data. Both the RMSE and MAPE of the SSA-Elman model are smaller than other models, with the smallest RMSE of 0.0097 and MAPE of 0.98%. The overall trend of the error is the same as in Table 7, but the reductions of the RMSE and MAPE values are more significant, reaching 0.0174 and 1.86% respectively. Numerically, it can be seen that the method proposed outperforms the Elman model in both accuracy and generalization. At the same time, the performance of the model proposed is also better than the LSTM model.

Finally, all the models are trained with 30% data, and Fig. 14 shows the outputs of Elman, LSTM and SSA-Elman. It can be seen from Fig. 14 that Elman and LSTM cannot accurately estimate the SOH with only 30% of the data for training, while the SSA-Elman model can continue to achieve SOH estimation because of the IUM. In addition, as shown in Fig. 14, because the training data is too small, the output of the Elman model has deviated from the decline trend of the true value. Compared with the Elman model, the LSTM model still maintains the same decline trend as the true value, but the error increases significantly after experiencing a capacity fluctuation. In contrast, the SSA-Elman model can continue to achieve SOH estimation because of the IUM. Although the SSA-Elman model also has accumulated errors, the errors are significantly smaller than with other methods. Thus, the proposed method shows clear advantages when the training data is insufficient.

The errors with 30% training data are shown in Table 9. As seen, the error of the SSA-Elman model is the smallest, with the minimum RMSE of 0.0386 and MAPE of 4.04%. Compared with the Elman model, the minimum RMSE of the SSA-Elman model is reduced by 0.0726, and the minimum MAPE is reduced by 9.50%. Thus, it proves that the IUM can significantly enhance the generalizability of the model.

From the results obtained by training the model with 70%, 50% and 30% data respectively, it is proved that the proposed features can support the model to achieve accurate estimation. Compared with Elman and LSTM, the SSA-Elman model has the smallest error and the highest accuracy. In addition, because of the addition of the IUM, the model proposed has good generalizability. Consequently, the SSA-Elman model can still achieve SOH estimation when trained with only 30% of the data.

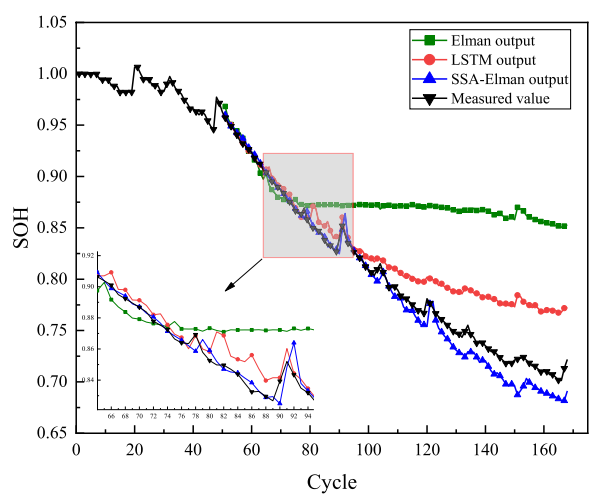

Fig. 14 The outputs of SSA-Elman, Elman and LSTM when using 30% training data

Table 8 The estimation error of 50% training data RMSE and MAPE

Method	B0005		B0006		B0007		B0018	
	RMSE	MAPE (%)	RMSE	MAPE (%)	RMSE	MAPE (%)	RMSE	MAPE (%)
Elman	0.0271	2.87	0.0480	4.93	0.0354	3.61	0.0476	4.66
LSTM	0.0202	2.11	0.0399	4.02	0.0347	3.23	0.0415	4.07
SSA-Elman	0.0097	1.01	0.0125	1.11	0.0107	1.01	0.0118	1.08

Table 9 The estimation error of 30% training data RMSE and MAPE

Method	B0005		B0006		B0007		B0018	
	RMSE	MAPE (%)	RMSE	MAPE (%)	RMSE	MAPE (%)	RMSE	MAPE (%)
Elman	0.1243	13.54	0.1702	16.58	0.1142	12.25	0.1674	16.99
LSTM	0.0884	9.67	0.1351	13.72	0.1027	11.09	0.1387	12.79
SSA-Elman	0.0386	4.04	0.0665	6.87	0.0416	2.35	0.0632	6.94

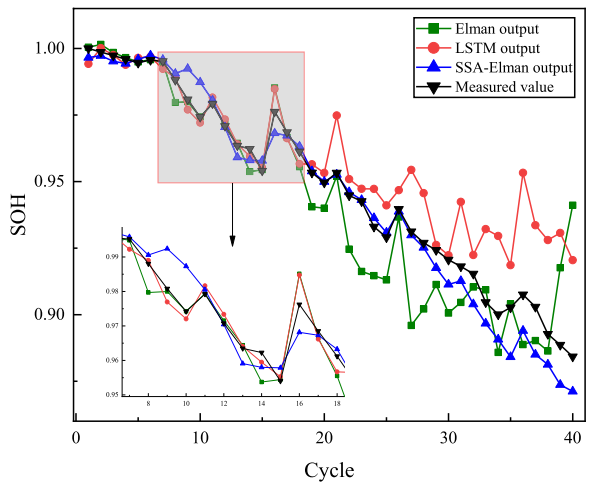

Fig. 15 Estimated results for battery B0046

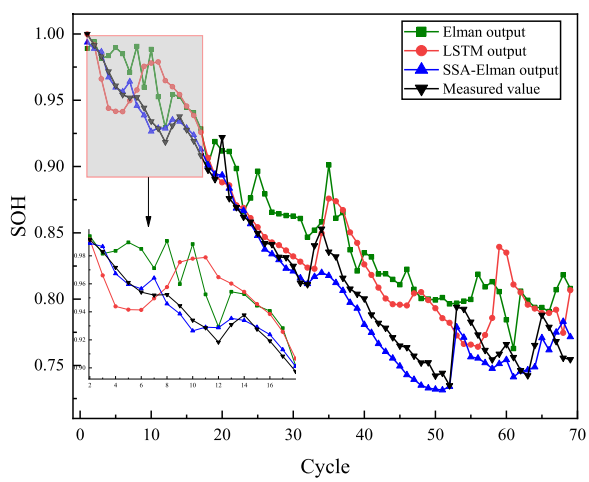

Fig. 16 Estimated results for battery B0029

4.5 High-temperature and low-temperature validation

High and low temperatures can significantly impact the lifetime of LIB, as well as the SOH estimation [55]. Therefore, the SSA-Elman model is further verified at high temperature and low temperature. In the low temperature experiment, B0046 is used as an example to show the estimation results, shown in Fig. 15. In the high temperature experiment, B0029 is used as an example and the estimation results are shown in Fig. 16. It can be seen from Figs. 15 and 16 that the proposed method can still estimate the SOH accurately, while the Elman model and the LSTM model can only estimate the overall downward trend of the SOH with large errors. This is because the IUM mechanism enables the model to fit the local variation of SOH well. In addition, the Ellman and LSTM models can still estimate the overall trend of SOH, which proves the effectiveness of the proposed features [56].

The estimated errors of the three batteries at low temperature are shown in Table 10, while Table 11 shows the estimated errors for the three batteries at high temperature. From the error data, it can be seen that the estimation accuracy of the proposed method is the highest, indicating that the estimation effect of the proposed method is superior to other common models. The estimation results of the three models are clearly higher at high temperature than at low temperature, because the capacity is more stable and the fluctuation is smaller at low temperature. When the battery capacity fluctuates greatly, the errors of the three models all increase, but the errors of the proposed model are all within acceptable ranges, e.g., RMSE is less than 0.0224 and MAPE is less than 2.21%. This proves that the proposed model can accurately estimate the SOH at high or low temperature.

Table 10 Estimation errors at low temperature

Method	B0046		B0047		B0048	
	RMSE	MAPE (%)	RMSE	MAPE (%)	RMSE	MAPE (%)
Elman	0.0363	3.90	0.0569	6.31	0.0849	3.95
LSTM	0.0318	3.18	0.0317	3.05	0.0414	2.63
SSA-Elman	0.0131	1.30	0.0224	2.21	0.0224	1.94

Table 11 Estimation errors at high temperature

Method	B0029		B0030		B0031	
	RMSE	MAPE (%)	RMSE	MAPE (%)	RMSE	MAPE (%)
Elman	0.0156	1.10	0.0245	1.99	0.0142	1.25
LSTM	0.0173	1.25	0.0106	0.80	0.0229	2.12
SSA-Elman	0.0076	0.59	0.0061	0.56	0.0064	0.58

5 Conclusion

It is of importance to estimate the SOH of LIBs. This paper presents a SOH estimation method based on the SSA-Elman model. After analyzing the aging principle and NASA dataset, five features are proposed. The correlations of these features are all above 0.99 after using the proposed MAD-SG filtering, while they can be extracted by only collecting the voltage and current in the charging stage without complex data processing. Finally, the performance of the proposed model is validated by different experiments at 24 °C, 43 °C and 4 °C using the NASA dataset, and is compared with the Elman model and LSTM model. The experimental results demonstrate that the features have good estimation performance and the method proposed outperforms both the Elman model and LSTM model in terms of accuracy and generalizability.

Abbreviations

LIB: Lithium-ion battery; OCV: Open circuit voltage; IC: Incremental capacity; MAPE: Mean absolute percentage error; IUM: Incremental update mechanism; SG: Savitzky–Golay; SEI: Solid electrolyte interphase; CV: Constant voltage; CEQ: Charged electric quantity; SOH: State of health; EIS: Electrochemical impedance spectroscopy; RMSE: Root mean square error; SSA: Sparrow search algorithm; PCoE: Prediction center of excellence; MAD: Median absolute deviation; CC: Constant current; VQA: V–Q area; PCT: Partial charging time.

Acknowledgements

This work was supported by the Youth Fund of Shandong Province Natural Science Foundation (No. ZR2020QE212), Key Projects of Shandong Province Natural Science Foundation (No. ZR2020KF020), the Guangdong Provincial Key Lab of Green Chemical Product Technology (GC202111), Zhejiang Province Natural Science Foundation (No. LY22E070007) and National Natural Science Foundation of China (No. 52007170).

Author contributions

The named authors have substantially contributed to conducting the underlying research and drafting this manuscript. All authors read and approved the final manuscript.

Funding

This work was supported by the Youth Fund of Shandong Province Natural Science Foundation (No. ZR2020QE212), Key Projects of Shandong Province Natural Science Foundation (No. ZR2020KF020), the Guangdong Provincial Key Lab of Green Chemical Product Technology (GC202111), Zhejiang Province Natural Science Foundation (No. LY22E070007) and National Natural Science Foundation of China (No. 52007170).

Availability of data and materials

The data and materials used to support the findings of this study are available from the corresponding author upon request.

Declarations

Competing interests

The authors declare that they have no known competing financial interests or personal relationships that could have appeared to influence the work reported in this paper.

Author details

[1]School of Electrical Engineering, Weihai Innovation Research Institute, Qingdao University, Qingdao 266000, China. [2]Xi'an Traffic Engineering Institute, Xi'an 710300, China. [3]Strategic Research Institute, State Power Investment Corporation, Beijing, China. [4]School of Information Engineering, Zhejiang University of Technology, Hangzhou, China.

Received: 6 May 2022 Accepted: 30 September 2022
Published online: 18 October 2022

References

1. Xu, H., Du, H., Kang, L., Cheng, Q., Feng, D., & Xia, S. (2021). Constructing straight pores and improving mechanical properties of gangue-based porous ceramics. *Journal of Renewable Materials, 9*(12), 2129–2141. https://doi.org/10.32604/jrm.2021.016090
2. Li, S., Hu, W., Cao, D., Dragicevic, T., Huang, Q., Chen, Z., & Blaabjerg, F. (2022). Electric vehicle charging management based on deep reinforcement learning. *Journal of Modern Power Systems and Clean Energy, 10*(3), 719–730. https://doi.org/10.35833/mpce.2020.000460
3. Marot, A., Kelly, A., Naglic, M., Barbesant, V., Cremer, J., Stefanov, A., & Viebahn, J. (2022). Perspectives on future power system control centers for energy transition. *Journal of Modern Power Systems and Clean Energy, 10*(2), 328–344. https://doi.org/10.35833/mpce.2021.000673
4. Chen, Z., Gao, Z., Chen, J., Wu, X., Fu, X., & Chen, X. (2021). Research on cooperative planning of an integrated energy system considering uncertainty. *Power System Protection and Control, 49*, 8. https://doi.org/10.19783/j.cnki.pspc.200876 in Chinese.
5. Xiong, R., Zhang, Y., Wang, J., He, H., Peng, S., & Pecht, M. (2019). Lithium-ion battery health prognosis based on a real battery management system used in electric vehicles. *IEEE Transactions on Vehicular Technology, 68*(5), 4110–4121. https://doi.org/10.1109/tvt.2018.2864688
6. Li, D., Yang, D., Li, L., Wang, L., & Wang, K. (2022). Electrochemical impedance spectroscopy based on the state of health estimation for lithium-ion batteries. *Energies, 15*, 6665. https://doi.org/10.3390/en15186665
7. Liu, Z., Jia, Z., Han, J., Yan, C., & Pecht, M. (2018). A patent analysis of prognostics and health management (PHM) innovations for electrical systems. *IEEE Access, 6*, 18088–18107. https://doi.org/10.1109/access.2018.2818114
8. Meriem, S. J., & Ines B. (2020). Lithium-ion battery pack modeling using accurate OCV model application for SoC and SoH estimation. In *2020 IEEE 4th international conference on intelligent energy and power systems (IEPS)* (175–179).
9. Topan, P. A., Ramadan, M. N., Fathoni, G., & Cahyadi, A. I. (2016). State of charge (SOC) and state of health (SOH) estimation on lithium polymer battery via Kalman filter. In *International conference on science and technology-computer (ICST)* (pp. 93–96).
10. Li, D., Wang, L., Duan, C., Li, Q., & Wang, K. (2022). Temperature prediction of lithium-ion batteries based on electrochemical impedance spectrum:

A review. *International Journal of Energy Research, 46*(8), 10372–10388. https://doi.org/10.1002/er.7905
11. Cui, Z., Dai, J., Sun, J., Li, D., Wang, L., & Wang, K. (2022). Hybrid methods using neural network and Kalman filter for the state of charge estimation of lithium-ion battery. *Mathematical Problems in Engineering*. https://doi.org/10.1155/2022/9616124
12. Coleman, M., Hurley, W. G., & Chin Kwan, L. (2008). An improved battery characterization method using a two-pulse load test. *IEEE Transactions on Energy Conversion, 23*(2), 708–713. https://doi.org/10.1109/tec.2007.914329
13. Matias, B., Anres, A., Juan, D. C., Perez, A., & Orchard, M. (2020). Remaining useful life of lithium-ion batteries as a function of the Joule effect. In *IEEE international autumn meeting on power, electronics and computing (ROPEC)* (pp. 1–6).
14. Bharat, B., & Mo-Yuen, C. (2015). The state of the art approaches to estimate the state of health (SOH) and state of function (SOF) of lithium ion batteries. In *IEEE 13th international conference on industrial informatics (INDIN)* (pp. 1302–1307).
15. Bartlett, A., Marcicki, J., Onori, S., Rizzoni, G., Yang, X. G., & Miller, T. (2015). Electrochemical model-based state of charge and capacity estimation for a composite electrode lithium-ion battery. *IEEE Transactions on Control Systems Technology*. https://doi.org/10.1109/tcst.2015.2446947
16. Saldana, G., Martin, J. I. S., Zamora, I., Asensio, F. J., Onederra, O., & Gonzalez, M. (2020). Empirical electrical and degradation model for electric vehicle batteries. *IEEE Access, 8*, 155576–155589. https://doi.org/10.1109/access.2020.3019477
17. Singh, P., Chen, C., Tan, C. M., & Huang, S. C. (2019). Semi-empirical capacity fading model for SoH estimation of Li-ion batteries. *Applied Sciences, 9*, 15. https://doi.org/10.3390/app9153012
18. Lai, X., Wang, S., Ma, S., Xie, J., & Zheng, Y. (2020). Parameter sensitivity analysis and simplification of equivalent circuit model for the state of charge of lithium-ion batteries. *Electrochimica Acta*. https://doi.org/10.1016/j.electacta.2019.135239
19. Cui, Z., Kang, L., Li, L., Wang, L., & Wang, K. (2022). A hybrid neural network model with improved input for state of charge estimation of lithium-ion battery at low temperatures. *Renewable Energy, 98*, 1328–1340. https://doi.org/10.1016/j.renene.2022.08.123
20. Yu, Z., Huai, R., & Li, H. (2021). CPSO-based parameter-identification method for the fractional-order modeling of lithium-ion batteries. *IEEE Transactions on Power Electronics, 36*(10), 11109–11123. https://doi.org/10.1109/tpel.2021.3073810
21. Li, D., Li, S., Zhang, S., Sun, J., Wang, L., & Wang, K. (2022). Aging state prediction for supercapacitors based on heuristic kalman filter optimization extreme learning machine. *Energy*. https://doi.org/10.1016/j.energy.2022.123773
22. Fang, L. L., Li, J. Q., & Peng, B. (2019). Online estimation and error analysis of both SOC and SOH of lithium-ion battery based on DEKF method. *Energy Procedia, 158*, 3008–3013.
23. Xia, Z. (2020). Evaluation of parameter variations of equivalent circuit model of lithium-ion battery under different SOH conditions. In *IEEE energy conversion congress and exposition (ECCE)* (pp. 1519–1523).
24. Liu, C., Zhang, Y., Sun, J., Cui, Z., & Wang, K. (2022). Stacked bidirectional LSTM RNN to evaluate the remaining useful life of supercapacitor. *International Journal of Energy Research, 463*, 3034–3043. https://doi.org/10.1002/er.7360
25. Cui, Z., Wang, L., Li, Q., & Wang, K. (2021). A comprehensive review on the state of charge estimation for lithium-ion battery based on neural network. *International Journal of Energy Research, 465*, 5423–5440. https://doi.org/10.1002/er.7545
26. Yi, Z., Zhao, K., Sun, J., & Wang, K. (2022). Prediction of the remaining useful life of supercapacitors. *Mathematical Problems in Engineering, 2022*, 1–8. https://doi.org/10.1155/2022/7620382
27. Tian, G., Gu, Y., Shi, D., Fu, J., Yu, Z., & Zhou, Q. (2021). Neural-network-based power system state estimation with extended observability. *Journal of Modern Power Systems and Clean Energy, 9*(5), 1043–1053. https://doi.org/10.35833/mpce.2020.000362
28. Jonata, C., Ronaldo, R. B., Milde, M. S., Lira, M. A., Ferreira, A., & Afonso de Carvalho, M. (2021). Power curve modelling for wind turbine using artificial intelligence tools and pre-established inference criteria. *Journal of Modern Power Systems and Clean Energy, 9*(3), 526–533. https://doi.org/10.35833/mpce.2019.000236
29. Ming, T., Zhao, J., Wang, X., & Wang, K. (2021). SOC estimation of a lithium battery under high pulse rate condition based on improved LSTM. *Power System Protection and Control, 49*, 8. https://doi.org/10.19783/j.cnki.pspc.200776 in Chinese.
30. Gou, B., Xu, Y., & Feng, X. (2020). State-of-health estimation and remaining-useful-life prediction for lithium-ion battery using a hybrid data-driven method. *IEEE Transactions on Vehicular Technology, 6910*, 10854–10867. https://doi.org/10.1109/tvt.2020.3014932
31. Severson, K. A., Attia, P. M., Jin, N., Perkins, N., Jiang, B., Yang, Z., Chen, M. H., Aykol, M., Herring, P. K., Fraggedakis, D., Bazant, M. Z., Harris, S. J., Chueh, W. C., & Braatz, R. D. (2019). Data-driven prediction of battery cycle life before capacity degradation. *Nature Energy, 45*, 383–391. https://doi.org/10.1038/s41560-019-0356-8
32. Li, Q., Li, D., Zhao, K., Wang, L., & Wang, K. (2022). State of health estimation of lithium-ion battery based on improved ant lion optimization and support vector regression. *Journal of Energy Storage*. https://doi.org/10.1016/j.est.2022.104215
33. Sun, H., Sun, J., Zhao, K., Wang, L., & Wang, K. (2022). Data-driven ICA-Bi-LSTM-combined lithium battery SOH estimation. *Mathematical Problems in Engineering, 2022*, 1–8. https://doi.org/10.1155/2022/9645892
34. Liu, D., Zhou, J. B., Liao, H. T., & Yu, P. (2015). A health indicator extraction and optimization framework for lithium-ion battery degradation modeling and prognostics. *IEEE Transactions on Systems, Man, and Cybernetics: Systems, 456*, 915–928. https://doi.org/10.1109/tsmc.2015.2389757
35. Bian, X., Wei, Z., He, J., Yan, F., & Liu, L. (2021). A novel model-based voltage construction method for robust state-of-health estimation of lithium-ion batteries. *IEEE Transactions on Industrial Electronics, 6812*, 12173–12184. https://doi.org/10.1109/tie.2020.3044779
36. Qu, W., Shen, W., & Liu, J. (2021). A joint grey relational analysis based state of health estimation for lithium ion batteries considering temperature effects. *Journal of Energy Storage*. https://doi.org/10.1016/j.est.2021.103102
37. Guo, Y., Yu, P., Zhu, C., Zhao, K., Wang, L., & Wang, K. (2022). A state-of-health estimation method considering capacity recovery of lithium batteries. *International Journal of Energy Reseach*. https://doi.org/10.1002/ER.8671
38. Liu, C., Li, D., Wang, L., Li, L., & Wang, K. (2022). Strong robustness and high accuracy remaining useful life prediction on supercapacitors. *APL Materials, 10*(6), 061106. https://doi.org/10.1063/5.0092074
39. Lin, D., Zhang, X., Wang, L., & Zhao, B. (2022). State of health estimation of lithium-ion batteries based on a novel indirect health indicator. *Energy Reports, 8*, 606–613. https://doi.org/10.1016/j.egyr.2022.02.220
40. Goebel, B. S. A. K. (2007). *"Battery data set", NASA ames prognostics data repository*. Moffett Field: NASA Ames Research Center. http://ti.arc.nasa.gov/project/prognostic-data-repository.
41. Gyenes, B., Stevens, D. A., Chevrier, V. L., & Dahn, J. R. (2014). Understanding anomalous behavior in coulombic efficiency measurements on Li-ion batteries. *Journal of The Electrochemical Society, 1623*, A278–A283. https://doi.org/10.1149/2.0191503jes
42. Lewerenz, M., Münnix, J., Schmalstieg, J., Käbitz, S., Knips, M., & Sauer, D. U. (2017). Systematic aging of commercial $LiFePO_4$/graphite cylindrical cells including a theory explaining rise of capacity during aging. *Journal of Power Sources, 345*, 254–263. https://doi.org/10.1016/j.jpowsour.2017.01.133
43. Li, X., Su, J., Li, Z., Zhao, Z., Zhang, F., Zhang, L., Ye, W., Li, Q., Wang, K., Wang, X., Li, H., Hu, H., Yan, S., Miao, G. X., & Li, Q. (2022). Revealing interfacial space charge storage of $Li^+/Na^+/K^+$ by operando magnetometry. *Science Bulletin, 6711*, 1145–1153. https://doi.org/10.1016/j.scib.2022.04.001
44. Hu, X., Xu, L., Lin, X., & Pecht, M. (2020). Battery lifetime prognostics. *Joule, 42*, 310–346. https://doi.org/10.1016/j.joule.2019.11.018
45. El Mejdoubi, A., Chaoui, H., Gualous, H., Van Den Bossche, P., Omar, N., & Van Mierlo, J. (2019). Lithium-ion batteries health prognosis considering aging conditions. *IEEE Transactions on Power Electronics, 347*, 6834–6844. https://doi.org/10.1109/tpel.2018.2873247
46. Birkl, C. R., Roberts, M. R., McTurk, E., Bruce, P. G., & Howey, D. A. (2016). Degradation diagnostics for lithium ion cells. *Journal of Power Sources, 341*, 373–386. https://doi.org/10.1016/j.jpowsour.2016.12.011
47. Hurriyatul Fitriyah, A. S. B. (2019). Outlier detection in object counting based on hue and distance transform using median absolute deviation (MAD). In *IEEE international conference on sustainable information engineering and technology (SIET)* (pp. 217–222).

48. Schafer, R. (2011). What is a Savitzky–Golay filter? [Lecture Notes]. *IEEE Signal Processing Magazine, 284*, 111–117. https://doi.org/10.1109/msp.2011.941097
49. Sun, W., & Wang, J. (2017). elman neural network soft-sensor model of conversion velocity in polymerization process optimized by Chaos Whale optimization algorithm. *IEEE Access, 5*, 13062–13076. https://doi.org/10.1109/access.2017.2723610
50. Chen, Z., Xue, Q., Xiao, R., & Liu, Y. (2019). State of health estimation for lithium-ion batteries based on fusion of autoregressive moving average model and Elman neural network. *IEEE Access, 7*, 102662–102678. https://doi.org/10.1109/access.2019.2930680
51. Cheng, Y. C., Qi, W. M., & Cai, W. Y. (2002). Dynamic properties of Elman and modified Elman neural network. In *International conference on machine learning and cybernetics* (pp. 637–640).
52. Ren, G., Cao, Y., Wen, S., Huang, T., & Zeng, Z. (2018). A modified Elman neural network with a new learning rate scheme. *Neurocomputing, 286*, 11–18. https://doi.org/10.1016/j.neucom.2018.01.046
53. Padhy, S., & Panda, S. (2021). Application of a simplified Grey Wolf optimization technique for adaptive fuzzy PID controller design for frequency regulation of a distributed power generation system. *Protection and Control of Modern Power Systems*. https://doi.org/10.1186/s41601-021-00180-4
54. Xue, J., & Shen, B. (2020). A novel swarm intelligence optimization approach: Sparrow search algorithm. *Systems Science & Control Engineering, 81*, 22–34. https://doi.org/10.1080/21642583.2019.1708830
55. Sun, H., Yang, D., Wang, L., & Wang, K. (2022). A method for estimating the aging state of lithium-ion batteries based on a multi-linear integrated model. *International Journal of Energy Research*. https://doi.org/10.1002/ER.8709
56. Cui, Z., Kang, L., Li, L. W., Wang, L. C., & Wang, K. (2022). A combined state-of-charge estimation method for lithium-ion battery using an improved BGRU network and UKF. *Energy, 259*, 124933. https://doi.org/10.1016/j.energy.2022.124933